Internal Kinematics and Structure of the Bulge Globular Cluster NGC 6569[*]

Cristina Pallanca[1,2] , Silvia Leanza[1,2] , Francesco R. Ferraro[1,2] , Barbara Lanzoni[1,2] , Emanuele Dalessandro[2] ,
Mario Cadelano[1,2] , Enrico Vesperini[3] , Livia Origlia[2] , Alessio Mucciarelli[1,2] , Elena Valenti[4,5] , and Andrea Miola[6]

[1] Dipartimento di Fisica e Astronomia, Università di Bologna, Via Gobetti 93/2 I-40129 Bologna, Italy; cristina.pallanca3@unibo.it
[2] INAF-Osservatorio di Astrofisica e Scienze dello Spazio di Bologna, Via Gobetti 93/3 I-40129 Bologna, Italy
[3] Department of Astronomy, Indiana University, Bloomington, IN, 47401, USA
[4] European Southern Observatory, Karl-Schwarzschild-Strasse 2, D-85748 Garching bei Munchen, Germany
[5] Excellence Cluster ORIGINS, Boltzmann-Strasse 2, D-85748 Garching Bei Munchen, Germany
[6] Dipartimento di Fisica e Scienze della Terra, Università di Ferrara, via Saragat 1, I-44122, Ferrara, Italy
Received 2023 February 22; revised 2023 April 4; accepted 2023 April 6; published 2023 June 16

Abstract

In the context of a project aimed at characterizing the properties of star clusters in the Galactic bulge, here we present the determination of the internal kinematics and structure of the massive globular cluster NGC 6569. The kinematics has been studied by means of an unprecedented spectroscopic data set acquired in the context of the ESO-VLT Multi-Instrument Kinematic Survey of Galactic globular clusters, combining the observations from four different spectrographs. We measured the line-of-sight velocity of a sample of almost 1300 stars distributed between $\sim 0\rlap{.}''8$ and $770''$ from the cluster center. From a subsample of high-quality measures, we determined the velocity dispersion profile of the system over its entire radial extension (from $\sim 5''$ to $\sim 200''$ from the center), finding the characteristic behavior usually observed in globular clusters, with a constant inner plateau and a declining trend at larger radii. The projected density profile of the cluster has been obtained from resolved star counts, by combining high-resolution photometric data in the center, and the Gaia EDR3 catalog radially extended out to $\sim 20'$ for a proper sampling of the Galactic field background. The two profiles are properly reproduced by the same King model, from which we estimated updated values of the central velocity dispersion, main structural parameters (such as the King concentration, the core, half mass, and tidal radii), total mass, and relaxation times. Our analysis also reveals a hint of ordered rotation in an intermediate region of the cluster ($40'' < r < 90''$, corresponding to $2r_c < r < 4.5r_c$), but additional data are required to properly assess this possibility.

Unified Astronomy Thesaurus concepts: Globular star clusters (656); Stellar dynamics (1596); Stellar kinematics (1608); Spectroscopy (1558)

Supporting material: machine-readable table

1. Introduction

The Galactic bulge is the sole spheroid where individual stars can be observed and for this reason is a formidable laboratory to study the processes that drive the formation of galaxy bulges. Unfortunately, because of observational limitations mainly related to the large extinction and stellar density in this direction of the sky, it still remains one of the most inaccessible regions of the Milky Way, and its structure, formation, and evolution are still subjects of intense debate in the literature (see, for example, Ness et al. 2013; Rich 2013; Origlia 2014; Zoccali & Valenti 2016; Johnson et al. 2022; Marchetti et al. 2022). In this respect the investigation of the globular clusters (GCs) orbiting the bulge is a key tool to trace the bulge properties in terms of kinematics, chemical abundances, and age (Bica et al. 2006; Valenti et al. 2007, 2010; Barbuy et al. 2018).

For this reason several years ago we initiated a systematic photometric and spectroscopic investigation of bulge GCs and their stellar populations (see Origlia et al. 1997, 2001, 2002; Origlia & Rich 2004; Origlia et al. 2005; Valenti et al. 2005, 2007; Ferraro et al. 2009; Valenti et al. 2010, 2011; Ferraro et al. 2015; Saracino et al. 2015, 2016; Cadelano et al. 2017b; Pallanca et al. 2019; Saracino et al. 2019; Cadelano et al. 2020; Pallanca et al. 2021b, 2021a; Cadelano et al. 2022; Leanza et al. 2022a; Deras et al. 2023). In this respect, the discovery that Terzan5 and Liller1 are not genuine GCs but host multi-iron and multiage stellar populations has opened a new line of investigation, providing the first detection of Bulge Fossil Fragments, the possible remnants of primordial giant clumps that contributed to the bulge formation, surviving the violent phase of its assembling (Ferraro et al. 2009; Lanzoni et al. 2010; Origlia et al. 2011, 2013; Massari et al. 2014; Ferraro et al. 2016; Origlia et al. 2019; Ferraro et al. 2021; Dalessandro et al. 2022).

In the framework of a complete kinematical, chemical, and photometric characterization of bulge GCs, the ESO-VLT Multi-Instrument Kinematic Survey (hereafter the MIKiS survey; Ferraro et al. 2018a, 2018b) is expected to provide an important contribution. The survey has been specifically designed to characterize the kinematical properties of a representative sample of Galactic GCs (GGCs) in different

Table 1
Spectroscopic Data Sets for NGC 6569

Name	Date	N_{exp}	t_{exp} (s)
MUSE/NFM			
C	2021-08-16	3	750
E	2021-08-16	3	750
N	2021-08-16	3	750
NE	2021-08-21	3	750
W	2021-08-21	3	750
SW	2021-08-21	3	750
S	2022-09-27	3	750
SINFONI			
LR_SW	2015-08-02	6	30
LR_W	2015-08-03	6	30
LR_N	2015-07-18	6	30
LR_NE	2016-07-22/2016-08-04	6	30
LR_S	2016-06-23	6	30
LR_NN	2016-07-15	6	30
LR_C	2015-08-23	6	30
LR_E	2016-07-21	12	30
KMOS			
kmos_1	2015-04-30	3	60
kmos_2	2015-05-02	3	60
kmos_3	2015-05-02	3	60
kmos_4	2015-05-02	3	60
kmos_faint_1	2015-05-02	3	100
kmos_faint_2	2015-05-02	3	100
kmos_faint_3	2015-05-02	3	100
kmos_faint_4	2015-05-03	3	100
kmos_faint_5	2015-05-02	3	100
FLAMES			
flames_HR13	2014-06-19/2014-08-01	2	2775
flames_HR21_faint_1	2015-06-22	1	1800
flames_HR21_faint_2	2015-07-26	1	1800
flames_HR21_faint_3	2015-07-26	1	1800
flames_HR21_veryfaint_1	2015-06-27	1	2700
flames_HR21_veryfaint_2	2015-06-27	1	2700
flames_HR21_VVfaint_2	2015-06-28/2015-07-26	2	2700

Note. For each of the data sets analyzed in this work (MUSE/NFM, SINFONI, KMOS and FLAMES), and for each individual pointing, the table lists the name, execution date, number of exposures (N_{exp}) and exposure time of each frame (t_{exp}, in seconds).

environments (halo and bulge) and in different dynamical evolutionary stages. The approach proposed in MIKiS is to derive both the velocity dispersion and the rotation profiles of the investigated systems from the line-of-sight velocities of a statistically significant sample of individual stars distributed over their entire radial extension. The survey was designed to exploit the remarkable performances of the spectroscopic capabilities currently available at the ESO Very Large Telescope (VLT). In particular, it uses the adaptive optics (AO) assisted integral field spectrograph SINFONI (operating in the infrared) and MUSE (in the optical band), the multi-object integral field spectrograph KMOS, and the multi-object, fiber-fed, and wide-field spectrograph FLAMES/GIRAFFE. The data set has been collected in the framework of three large programs (namely 193.D-0232, 195.D-0750, 106.21N5, PI: Ferraro; the last one is still ongoing), complemented with a

series of specific proposals. Some recent results can be found in Ferraro et al. (2018a), Lanzoni et al. (2018a, 2018b), and Leanza et al. (2022b). When possible, this approach is also complemented with accurate measures of individual proper motions (PMs; see Massari et al. 2013; Cadelano et al. 2017a; Libralato et al. 2018; Raso et al. 2020; Libralato et al. 2022).

In this paper, we present the velocity dispersion profile of NGC 6569, a massive GC (with absolute total magnitude $M_V = -8.3$) located in the Sagittarius region ($l = 0°.48$, $b = -6°.68$; Harris 1996) of the Galactic bulge, at a distance of ~3 kpc from the Galactic center (Harris 1996). The cluster is projected toward the dark nebula Barnard 305 (Barnard et al. 1927), and it is therefore highly reddened, with an average color excess $E(B - V) = 0.53$ (Ortolani et al. 2001). It is an intermediate/high, metal-rich cluster, with a quoted metallicity ranging from $[Fe/H] = -0.79 \pm 0.02$ (Valenti et al. 2011) to $[Fe/H] = -0.87$ (Johnson et al. 2018), and with an α-element enhancement of $[\alpha/Fe] = +0.4$ (Valenti et al. 2011). This system has been subject to a detailed photometric analysis by our group (see Saracino et al. 2019) by using a combination of optical Hubble Space Telescope/WFC3 data and multi-conjugate adaptive optics assisted near-infrared (NIR) GEMINI observations. This allowed an accurate measure of PMs, which provided a robust selection of cluster member stars. A differential reddening map has been also derived. The PM-selected and the differential reddening corrected color–magnitude diagram (CMD) then has allowed an accurate measure of the cluster distance and age: the distance modulus is $(m - M)_0 = 15.03 \pm 0.08$, corresponding to 10.1 ± 0.2 kpc from the Sun, while the age amounts to about 12.8 Gyr, with an uncertainty of 0.8–1.0 Gyr (Saracino et al. 2019).

The paper is organized as follows. In Section 2 we present the observations and describe the procedures adopted for the data reduction. In Section 3 we discuss the selection of the samples, the methods to determine the radial velocities (RVs), and the strategy adopted to homogenize the different data sets available. The results are presented in Section 4, while Section 5 is devoted to the discussion and conclusions.

2. Observations and Data Reduction

As anticipated in the Section 1, to build the velocity dispersion profile of NGC 6569 we used a multi-instrument approach combining the RV measurements obtained from four different spectroscopic data sets.

MUSE/NFM—The innermost cluster regions were sampled mainly by using the AO-assisted integral field spectrograph MUSE in the narrow field mode (NFM; Bacon et al. 2010). This is the MUSE configuration that provides the highest spatial resolution. MUSE at ESO-VLT consists of a modular structure composed of 24 identical integral field units (IFUs), and in the NFM configuration, it is equipped with the AO facility (AOF) of the VLT and the GALACSI-AO module (Arsenault et al. 2008; Ströbele et al. 2012). At the highest spatial sampling ($0''.025 \, pixel^{-1}$), MUSE/NFM observations cover a field of view of $7''.5 \times 7''.5$, which is smaller than that provided by the wide-field mode (WFM) configuration ($1' \times 1'$, with a sampling of $0''.2 \, pixel^{-1}$). MUSE provides a wavelength coverage from 4800 Å to 9300 Å, with a resolving power $R \sim 3000$ at $\lambda \sim 8700$ Å. Our data set has been collected as part of the ESO Large Program ID: 106.21N5.003 (PI: Ferraro; see Table 1) and consists of a mosaic of seven MUSE/NFM pointings sampling the innermost ~15″ from

the center. Three 750 s long exposures were acquired for each pointing, with an average DIMM seeing always better than $\sim 0\rlap{.}''7$. A small dithering pattern and a rotation offset of 90° were secured between consecutive exposures of the same pointing in order to remove possible systematic effects between the individual IFUs. The data reduction was performed with the dedicated MUSE ESO pipeline (Weilbacher et al. 2020). It performs the basic reduction (bias subtraction, flat-fielding, and wavelength calibration) for each individual IFU, then applies the sky subtraction and transforms the preprocessed data into physical quantities by performing the flux and astrometric calibration for each IFU and applying the heliocentric velocity correction to all the data. In the next step, the data from all 24 IFUs are combined into a single datacube, and, finally, the pipeline combines the data cubes of the multiple exposures of each pointing into a final single datacube, taking into account the dithering offsets and rotations among different exposures.

SINFONI—To sample the innermost regions, we also used an additional spectroscopic data set acquired with the NIR (1.1–2.45 μm) AO-assisted integral field spectrograph SINFONI (Eisenhauer et al. 2003) at the ESO-VLT. The observations (ESO Large program ID: 195.D-0750(A), PI: Ferraro) were performed with the *K*-band grating, which samples the wavelength range 1.95–2.45 μm and provides a spectral resolution $R \sim 4000$, with a spatial scale of $0\rlap{.}''25$ spaxel^{-1} corresponding to a field of view of $8'' \times 8''$. The data set is listed in Table 1 and includes eight pointings covering a region of $\sim 15''$ from the cluster center. For each pointing, multiple exposures (usually six) were acquired on the target and on a sky region following a typical target–sky sky–target sequence in order to allow an adequate subtraction of the background. The observations have been executed adopting an exposure time of 30 s and under an average DIMM seeing of $\sim 0\rlap{.}''8$. The data reduction was performed by using the standard ESO pipeline (esorex 3.13.6) following the workflow 3.3.2 under the EsoReflex environment (Freudling et al. 2013). In the first step, the pipeline applies the corrections for darks, flats, and geometrical distortions to all the target and sky exposures. Then, it subtracts the sky background and performs the wavelength calibration. Finally, the processed target frames are combined in a datacube for each exposure.

KMOS—The cluster region at intermediate distances from the center has been sampled by using the integral field spectrograph KMOS (Sharples et al. 2013) at the ESO-VLT. KMOS employs 24 IFUs, each one with a field of view of $2\rlap{.}''8 \times 2\rlap{.}''8$ and a spatial sampling of $0\rlap{.}''2$ pixel^{-1}. The IFUs can be allocated within a $7\rlap{.}'2$ diameter field of view. The data have been acquired under the ESO Large Program ID: 193.D-0232 (PI: Ferraro) adopting the YJ grating, which samples the 1.025–1.344 μm spectral range at a resolution $R \sim 3400$, and with the spectral sampling of ~ 1.75 Å pixel^{-1}. Nine pointings (see Table 1) were acquired within $\sim 3'$ from center. Four pointings consist of a sequence of three repeated subexposures, each one 60 s long; the other five pointings are a set of three longer (100 s long) repeated subexposures that were acquired to sample fainter stars. The spectroscopic targets have been selected from the NIR catalog described in Valenti et al. (2005, 2007),[7] complemented, in the outermost regions of the clusters, with data from the 2MASS catalog (Skrutskie et al. 2006). Typically, the KMOS observations were planned to

have one/two red giant branch (RGB) stars in the field of view of each IFU (see also Lapenna et al. 2015). The data reduction has been performed by adopting the dedicated ESO pipeline,[8] executing background subtraction, flat-field correction, and wavelength calibration.

FLAMES—To investigate the cluster kinematics in the outermost cluster regions we used the fiber-fed multi-object spectrograph FLAMES (Pasquini et al. 2002) in the GIRAFFE/MEDUSA mode, which consists of 132 fibers with an aperture of $1\rlap{.}''2$ each. The observations have been executed adopting the HR21 and HR13 grating setups (ESO Large Program ID: 193.D-0232(F), PI: Ferraro, and ID: 093.D-0286 (A), PI: Villanova, respectively; see Table 1). The HR13 data set samples the spectral range 6120–6405 Å with a resolving power $R \sim 26{,}400$ and consists of two repeated exposures (each 2775 s long) of the same targets. The HR21 grating provides a resolving power $R \sim 18{,}000$ sampling the wavelength range between 8484 and 9001 Å. The targets have been selected to sample the full extension in the luminosity of the RGB. Thus, six pointings were planned to optimize the observations of targets with different luminosities: the brightest portion of the RGB has been sampled through three pointings (each with a 1800 s long exposure), while two pointings with an exposure time of 2700 s were devoted to observe intermediate-luminosity RGB stars, and finally an additional pointing of 5400 s was dedicated to sample the fainter portion of the RGB. As for the KMOS data set, the targets have been selected from the SOFI/2MASS photometric catalogs by sampling the full extension along the cluster RGB, and the data have been reduced with the dedicated ESO pipelines.[2]

3. Center of Gravity

For a proper analysis of the density and RV distributions of stars in NGC 6569, the first step is the determination of the center of gravity of the cluster. To this aim, we used the photometric catalog described in Saracino et al. (2019). This is based on F555W and F814W images obtained from high-resolution Hubble Space Telescope (HST)/WFC3 observations and a set of *J*- and K_s-band images acquired with the Gemini Multi-Conjugate Adaptive Optics System (GeMS). The field of view of the GeMS observations is almost entirely included within that of the HST/WFC3 images, which extend out to $\sim 150''$ from the center (see Figure 2 of Saracino et al. 2019). As in previous papers, we have determined the position of the gravitational center (C_{grav}) from the position of resolved stars (in the HST data set), rather than the surface brightness peak. This is done to avoid possible biases induced by the presence of a few bright stars, which could significantly offset the location of the surface brightness peak, with respect to the real C_{grav}.

To identify the position of C_{grav}, we adopted the iterative procedure described in Montegriffo et al. (1995) and used in many other papers (see, e.g., Lanzoni et al. 2010; Miocchi et al. 2013; Lanzoni et al. 2019; Cadelano et al. 2020; Pallanca et al. 2021b). This method computes the position of C_{grav} by averaging the projected coordinates (x, y) on the plane of the sky of a sample of resolved stars selected in an appropriate range of magnitude and within a given radial distance (r) from the center, starting from a first-guess value of the latter. Among the targets of the photometric catalog described in Saracino

---

[7] The catalog is available at the website http://www.bo.astro.it/~GC/ir_archive/.

[8] http://www.eso.org/sci/software/pipelines/

et al. (2019), we considered only the stars brighter than $m_{\rm F814W} = 20.0$, 20.3, and 20.6, which are reasonable selections to obtain statistically large samples while avoiding incompleteness effects. For each magnitude cut, we considered the stars included within circles of different radii ($r = 30''$, $r = 34''$, and $r = 38''$) from the adopted center. These values are larger than the cluster core radius quoted in the literature ($r_c = 21''$; Harris 1996) to ensure that the procedure is applied in a region where the density profile starts to decrease (see Miocchi et al. 2013). As the first-guess center we adopted the value quoted in Harris (1996). Then, from each subsample of selected stars we computed a new guess value of the cluster center by averaging the stellar coordinates projected on the plane of the sky. The procedure is repeated iteratively by using each time the center value computed in the previous iteration, until convergence. The convergence is reached when ten consecutive iterations provide values of the center that differ by less than $0''01$ from each other. We determined the final position of $C_{\rm grav}$ of NGC 6569 as the average of the values obtained from each subsample, finding $\alpha = 18^{\rm h}13^{\rm m}38^{\rm s}70$, $\delta = -31°49'37''13$, with an uncertainty of $\sim 0''3$. This is located at $\sim 0''1$ west and $\sim 0''3$ south from the previous estimate reported in Harris (1996). In the next analysis, we always adopted the position of the cluster center obtained in this work.

4. Radial Velocity Measurements

To properly derive the RV of individual stars from the spectra acquired with the four different spectrographs used in this work, we have performed a specific analysis of each data set following a procedure similar to the one described in Leanza et al. (2022b). Below we summarize only the main steps.

MUSE—The MUSE spectra have been extracted by using the software PampelMuse (Kamann et al. 2013), which allows us to obtain deblended source spectra of individual stars even in crowded regions of stellar systems, by performing a wavelength-dependent point-spread function (PSF) fitting. PampelMuse uses as input a reference catalog with the magnitudes and the coordinates of all the stars present in the field of view of the datacube. For this purpose we adopted the photometric catalog obtained by Saracino et al. (2019). As the PSF model we selected the MAOPPY function (Fétick et al. 2019), which was developed to properly reproduce both the core and the halo of the AO-corrected PSF in MUSE/NFM observations (for more details, see Göttgens et al. 2021). Briefly, for each slice of the MUSE datacube, PampelMuse fits the PSF and a coordinate transformation from the reference catalog to the data and uses these quantities to extract the spectra of all the stars in the datacube optimizing the deblending of the sources. The RV measures have been derived from the Doppler shifts of the Calcium Triplet lines in the wavelength range 8450–8750 Å by following the same procedure described in the previous paper (Leanza et al. 2022b). To this aim, a library of synthetic spectra computed with the SYNTHE code has been used. The template spectra have been produced in the wavelength range covered by MUSE, adopting the cluster metallicity with an α-enhanced chemical mixture ([Fe/H] = -0.79 dex and [α/Fe] = 0.4 dex, respectively; Valenti et al. 2011) and appropriate atmospheric parameters (effective temperature and gravity), according to the evolutionary phase of the targets, and applying a convolution with a Gaussian profile to obtain the MUSE spectral resolution.

Briefly, the procedure first normalizes the spectra corrected for heliocentric velocity to the continuum, which is estimated by a spline fitting of the spectrum in an appropriate wavelength range. Then, it computes the residuals between the normalized observed spectra and each template of the library, shifted in RV by steps of 0.1 km s^{-1} in an appropriate velocity range. By determining the smallest standard deviation in the distribution of the residuals, the procedure then provides, as a result, the best-fit synthetic spectrum (hence, the best estimates of temperature and gravity), and the RV of the target. An estimate of the signal-to-noise ratio (S/N) of the spectrum is also computed as the ratio between the average of the counts and their standard deviation in the wavelength range 8000–9000 Å. The top left panel of Figure 1 shows an example of the output of this procedure. For stars with different atmospheric parameters (the estimated effective temperature is labeled) and in the wavelength range used to estimate the RV, each panel shows the observed spectrum (in black) and the best-fit synthetic spectrum shifted by the estimated RV (color). The RV uncertainties have been determined by running 9000 Monte Carlo simulations of spectra with S/N between 10 and 90 and applying to these simulated spectra the same procedure used for the observed ones (for more details, see Leanza et al. 2022b). The typical RV errors are lower than 2 km s^{-1} for the brightest stars and increase as a function of the magnitude up to ~ 8 km s^{-1}, as shown in Figure 2 (top left panel). In the case of overlapping MUSE pointings, the stars in common have been used to search for possible systematic offsets in the RV measures, always finding a good agreement within the errors. In the case of stars with multiple exposures, we performed a weighted mean of all the RV measures by using the individual errors as weights. In total we obtained RV measures for a sample of 475 targets. The position of these targets in the plane of the sky is plotted in Figure 3, while the color scale shows the magnitude range covered by the sample.

SINFONI—The method adopted for the extraction and the analysis of the SINFONI spectra has been shortly presented in Leanza et al. (2022b) and will be extensively described in a forthcoming paper (C. Pallanca et al. 2023, in preparation). SINFONI spectra have been extracted from all the spaxels showing photon counts above a fixed threshold that was assumed at 10σ from the background level. RVs were then computed by following a procedure analogous to that applied for the MUSE spectra. In the case of SINFONI, we used the ^{12}C^{16}O band heads as reference lines to determine the Doppler shift. The set of synthetic spectra has been computed with the SYNTHE code (Sbordone et al. 2004; Kurucz 2005) adopting temperature and surface gravity typical of RGB stars, metallicity and α-element abundances of the cluster (Valenti et al. 2011). The synthetic spectra have been computed to cover the same NIR wavelength range covered by the SINFONI observations with the same spectral resolution (by means of a convolution with a Gaussian profile). Moreover, since the deepness of the CO band heads severely depends on both the chemical abundance and the temperature, as shown by the example in the top right panel of Figure 1, and stars above the RGB bump could be depleted in carbon, we computed seven additional synthetic spectra with appropriate carbon depletion [C/Fe] = -0.27 dex (Valenti et al. 2011) and different values of the atmospheric parameters to properly reproduce the brightest portion of the RGB, above the RGB bump. As mentioned above, to obtain the RVs we applied the
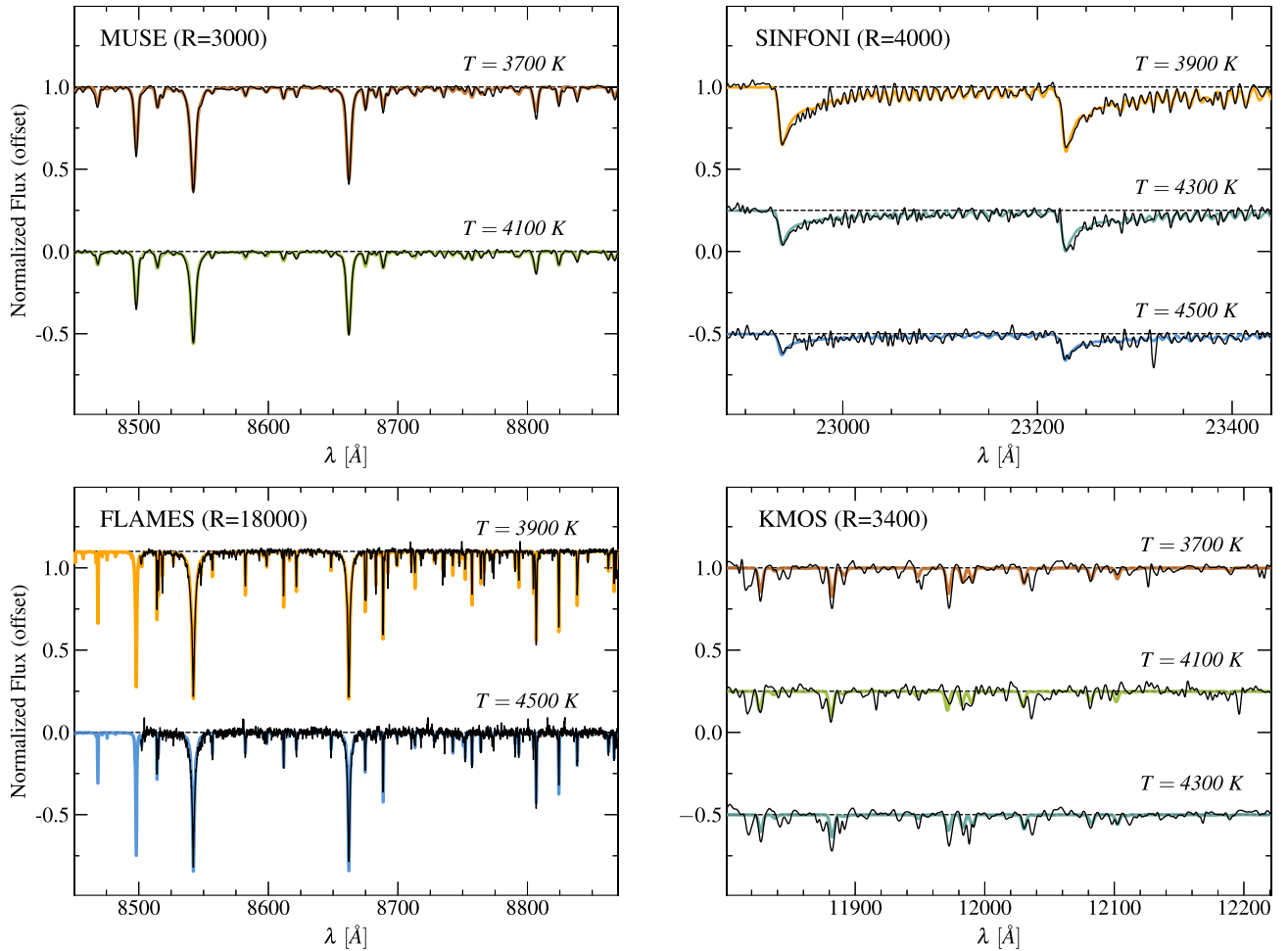
Figure 1. Examples of normalized observed spectra (in black) of stars with different atmospheric parameters, acquired with MUSE/NFM (top left), SINFONI (top right), FLAMES in the HR21 setup (bottom left), and KMOS (bottom right). For each observed spectrum, the best-fit synthetic spectrum obtained from the procedures described in Section 4 and shifted by the derived RV value is overplotted in color according to the effective temperature (labeled for each spectrum) associated to the best-fit template. The difference in the spectral resolution (labeled in each panel) of the various instruments is evident, as it is also the temperature dependence of the CO band head deepness in the SINFONI spectra.

same procedure used for the MUSE data, and also the RV uncertainties have been estimated from similar Monte Carlo simulations. The errors obtained are of the order of 2 km s^{-1}, and also in this case, they display a trend with the magnitude (see the bottom left panel of Figure 2). No significant offsets have been detected by comparing the RV measures of stars in common between different overlapping pointings. At the end of this procedure we merged the measures obtained from all the pointings by adopting as final value of RV for each star the weighted average of all the multiple measures using the estimated errors as weights. Since the SINFONI data set covers the overcrowded, innermost regions of the cluster and no deblending procedures similar to those implemented in PampelMuse are available in this case, it is important to evaluate the effect on the RV measures of the possible contamination of the spectra from the light coming from bright neighboring stars. For this reason, for each target we estimate the contamination parameter (C, see Leanza et al. 2022a). This is defined as the ratio between the fraction of "contaminating light" with respect to the contribution of the target itself in the central spaxel. The "contaminating light" is estimated as the expected photon counts from the neighboring sources providing the largest contribution to the central spaxel, and it is

estimated on the basis of the PSF model that best reproduces the SINFONI data and the list of stellar sources from the HST/GeMS catalog. In order to select only the safest targets with negligible contamination from the light of neighboring sources, we selected only the SINFONI targets with $C < 0.03$. The final sample consists of 51 targets, which are all bright stars.

FLAMES—For the FLAMES spectra, we determined the RVs from the Doppler shift of atomic lines in the wavelength ranges 6200–6350 Å and 8520–8870 Å for the HR13 and HR21 data sets, respectively. Also in this case, the library of template spectra has been computed with the SYNTHE code (Sbordone et al. 2004; Kurucz 2005) in the appropriate wavelength range adopting the cluster metallicity and different atmospheric parameters sampling the entire RGB extension. The RV uncertainties have been derived as in the previous cases, by means of Monte Carlo simulations, obtaining typical errors of the order of 0.5 km s^{-1} thanks to the higher spectral resolution. The top right panel of Figure 2 shows that the RV errors have a roughly constant trend as a function of the magnitude of the stars in place of the typical increasing trend seen for the other data sets. This is because faint stars have been observed with longer exposure times, thus keeping the S/N (and the uncertainties) almost constant at all magnitudes.
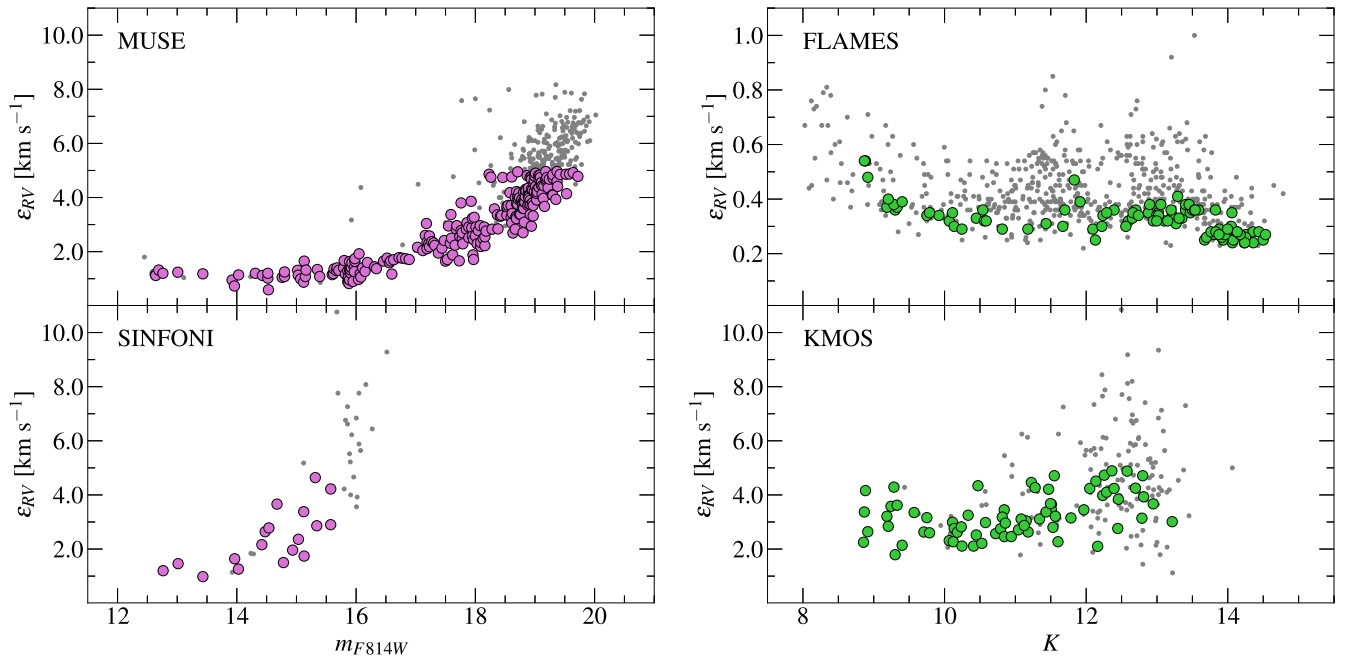
Figure 2. RV uncertainty (ϵ_{RV}) as a function of the star magnitude for the stars observed in the MUSE/NFM, SINFONI, FLAMES, and KMOS data sets (top left, bottom left, top right, and bottom right panels, respectively; see labels). In all panels, the colored circles correspond to the targets surviving the membership and the quality selections (see Section 5), while the gray dots are the stars rejected from the analysis.

We obtained a final FLAMES sample of 680 RV measures. The position of the target stars in the plane of the sky is shown in the bottom right panel of Figure 3, in which the color scale represents the magnitude.

KMOS—For the KMOS data set, the RVs have been measured by adopting the procedure described in Lapenna et al. (2015) and Ferraro et al. (2018a, 2018b). The spectra have been extracted from the central and most exposed spaxel of each target star identified in the field of view of each IFU. Then, by using the FXCOR task under the software IRAF, the spectra corrected for heliocentric velocity have been cross-correlated with appropriate synthetic spectra, according to the method described in Tonry & Davis (1979). As for the other data sets, the synthetic spectra have been obtained with the SYNTHE code (Sbordone et al. 2004; Kurucz 2005) using the wavelength range and the spectral resolution adequate for KMOS, and the uncertainties have been computed using similar Monte Carlo simulations. The derived errors are of about 3 km s^{-1}, and they show the trend with the magnitude plotted in the bottom right panel of Figure 2. As described above, consistent methods have been used to measure the RVs of the MUSE, SINFONI, and FLAMES targets, while a cross-correlation technique has been adopted in the case of KMOS spectra. Hence, to ensure that this introduced no systematics, we redetermined the RVs of a subsample of control stars observed with MUSE, SINFONI, and FLAMES by using the cross-correlation implemented in IRAF. In all cases, we obtained RV values in excellent agreement with the previous determinations. The final KMOS catalog consists of 220 RV measures. The bottom left panel of Figure 3 shows the target's position on the plane of the sky with respect the cluster center and the sampled magnitude range.

4.1. Final Catalog

To produce a homogeneous final catalog, we checked for possible systematic offsets in RV among the different spectroscopic data sets. Adopting the FLAMES RVs as reference, because of the highest spectra resolution of this instrument, we compared the RV values of the stars in common between each pair of data sets using only the most reliable measures. We detected and applied the following offsets to realign all the measures on the FLAMES values: shift of −2.4 km s^{-1} has been applied to all the KMOS RVs, 1.9 km s^{-1} to the MUSE values, and −0.5 km s^{-1} to the SINFONI measures. Moreover, to check whether the RV uncertainties are properly estimated, we used the velocity measures (v_1 and v_2) of the targets observed in multiple data sets and their associated errors (ϵ_1 and ϵ_2) to derive the quantity

$$\delta v_{1,2} = \frac{v_1 - v_2}{\sqrt{\epsilon_1^2 + \epsilon_2^2}}, \tag{1}$$

which should return a normal distribution with a standard deviation of 1 in the case of correct uncertainties (see also Kamann et al. 2016). To have a large enough sample of repeated measures, we used the stars in common between FLAMES and KMOS and between MUSE and SINFONI, obtaining in both cases distributions consistent with a normal function with a standard deviation of ∼1, thus guaranteeing that the errors are correctly estimated.

Then, to create the final catalog, we combined the four data sets previously homogenized by averaging the RV values of the targets with multiple measures using the estimated errors as weights. We obtained a final sample of 1292 RVs of individual stars distributed from 0″.8 to 723″.7 from the cluster center (corresponding to ∼1.2 times the truncation radius $r_t = 589$″.7; see Section 7). Figure 4 shows the position of the targets in the optical and NIR CMDs for the internal (MUSE and SINFONI) and external (FLAMES and KMOS) samples, respectively.
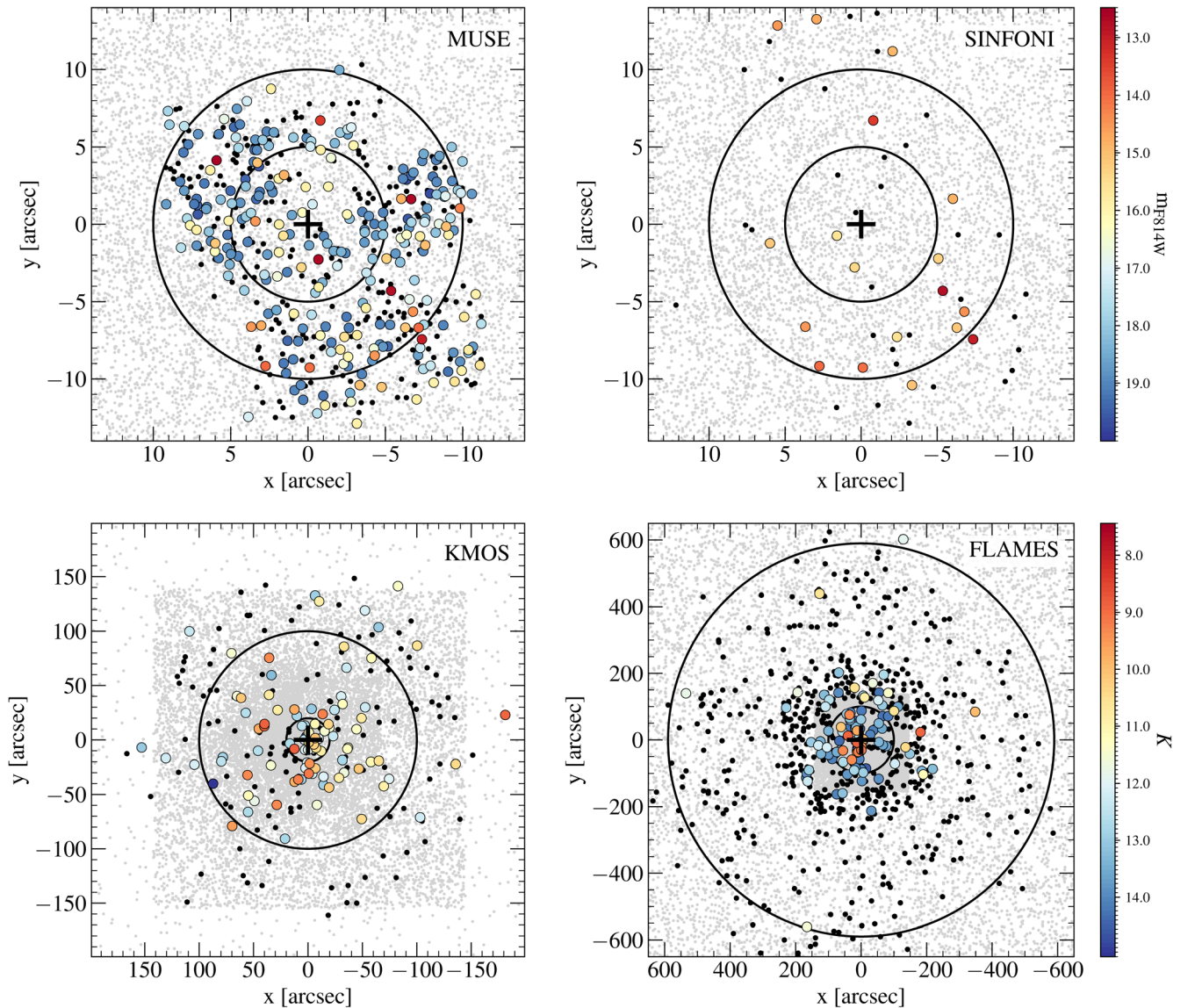
Figure 3. Maps in the plane of the sky, with respect to the adopted cluster center (black cross, determined in Section 3), of the stars with measured RV in each data set. In all panels, the colored circles mark the targets that survived the membership and quality selections and have been used for the kinematic analysis (see Section 5), while the black dots are the rejected stars. The color scales indicate the $m_{\rm F814W}$ and K-band magnitudes for the inner sample (MUSE and SINFONI, top panels) and for the external data sets (KMOS and FLAMES, bottom panels), respectively. Top left: focus on the central region sampled by MUSE. The gray dots are the stars of the HST/GeMS photometric catalog (Saracino et al. 2019). The two circles mark distances of 5″ and 10″ from the center. Top right: as in the top left panel but relating to the SINFONI data set. Bottom left: map relative to the position of the KMOS targets. The gray dots in the background mark the stars in the SOFI/2MASS catalog. The two circles are centered in the cluster center and have radii of 19″.9 (equal to the core radius of the cluster; see Section 7) and 100″. Bottom right: external portion of the cluster sampled by the FLAMES targets. The gray dots are as in the bottom left panel, while the two circles mark distances of 100″ and 589″.7 (corresponding to the truncation radius of the cluster; see Section 7) from the center.

5. Internal Kinematics

5.1. Cluster Membership

In order to properly study the internal kinematics of the cluster, we have performed an accurate selection of member stars among the targets of our final catalog. To obtain the most reliable cluster membership selection, we used a combination of PMs provided by the Gaia EDR3 (Gaia Collaboration et al. 2016, 2021) and the relative PMs measured by Saracino et al. (2019). In particular, for the external sample (FLAMES and KMOS), we adopted the Gaia PMs by selecting as cluster members the targets with magnitude $G < 19$ and PMs within 0.5 mas yr^{-1} from the absolute PM of the cluster (Vasiliev & Baumgardt 2021) in the vector-point diagram (VPD). The Gaia

VPD and the member selection of the external sample are shown in the top right panel of Figure 5. Most of the targets of the inner sample (MUSE and SINFONI), instead, are located in regions too crowded to allow reliable Gaia PM measures. We thus used the relative PMs obtained by Saracino et al. (2019) from the combination of HST and GeMS observations secured at two different epochs. In selecting member stars for this sample we followed the prescriptions described in Saracino et al. (2019): the targets of the internal sample selected as member stars are shown with large magenta circles in the VPD of the relative PMs in the top left panel of Figure 5. The efficiency of the adopted PM selection in excluding field stars is evident from the bottom panel of Figure 5, which shows the target RVs as a function of the distance from the center, with
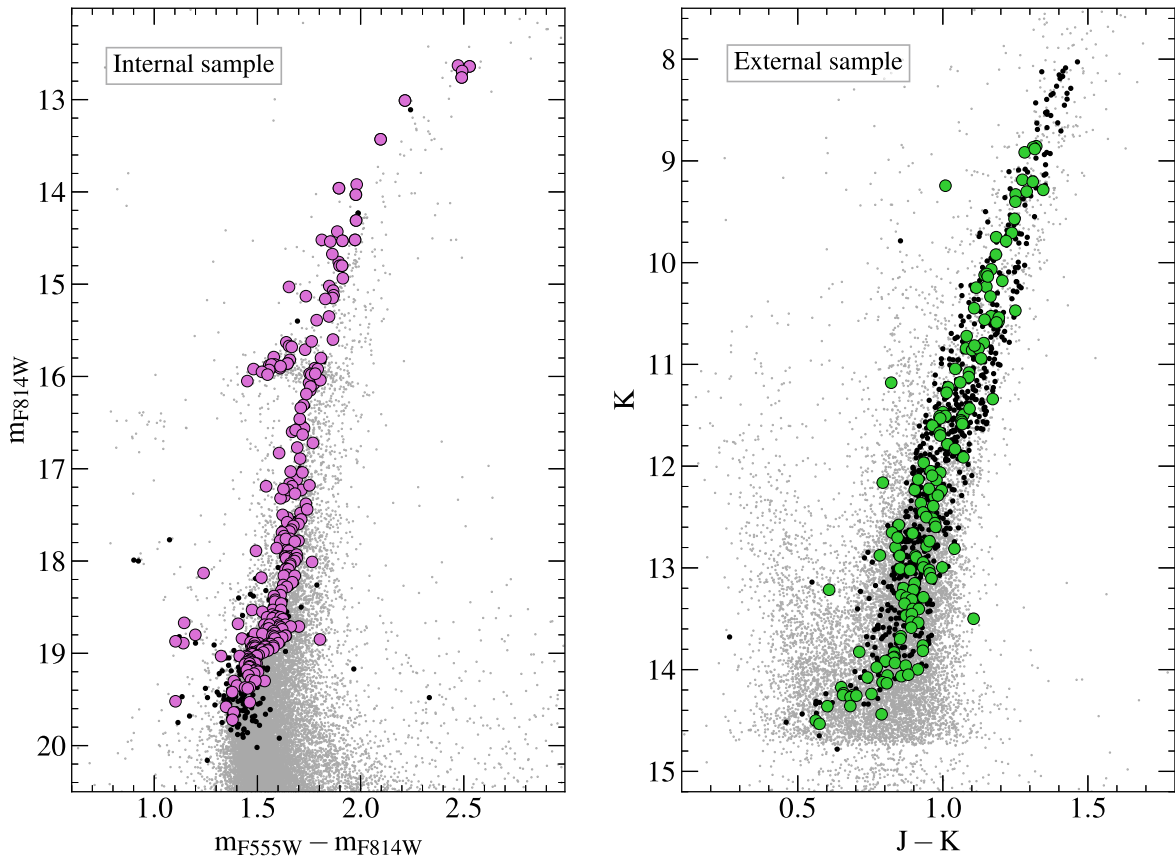
Figure 4. CMDs of NGC 6569 showing the targets of the final kinematic catalog. Left panel: HST optical CMD (gray dots, from Saracino et al. 2019) with the targets of the internal sample (MUSE and SINFONI) highlighted. The large magenta circles mark the targets after all the membership and quality selections described in Section 5, while the black dots are the rejected targets. Right panel: the gray dots show the $(K, J-K)$ CMD obtained from the SOFI/2MASS catalog. The large green circles and black dots are, respectively, the targets of the external sample (KMOS and FLAMES) selected for the kinematic analysis and those rejected on the basis of the adopted membership and quality selections.

the stars selected as cluster members marked with colored large circles. After this selection, the bulk of cluster members is centered at about -48 km s^{-1}, while the number of contaminating field stars (gray dots in the figure) is significant at larger radii and become dominant in the outermost regions. The remaining obvious outliers have been removed in the following analysis, according to their RV. With the purpose to perform a precise kinematic analysis, we also adopted additional criteria to select the targets with the most reliable RV measurements.[9] Therefore, for the following analysis, we used only the cluster member targets with S/N >15 and RV error <5 km s^{-1} (see their position on the plane of the sky and in the CMDs in Figures 3 and 4, respectively).

5.2. Systemic Velocity

For the determination of the systemic velocity ($V_{\rm sys}$) of NGC 6569, among the targets selected with the criteria described above, we conservatively adopted additional cuts in RVs (-80 km s^{-1} $<$ RV < -20 km s^{-1}) and applied a 3σ-clipping algorithm to the remaining distribution, thus minimizing the risk of residual field contamination. The RVs of the resulting sample (made of 393 stars) are plotted as black circles as a function of the distance from the center in the left panel of Figure 6, while their

distribution is drawn as a filled gray histogram in the right panel, with the peak indicating the systemic velocity of the cluster. Assuming a Gaussian RV distribution, we determined the value of $V_{\rm sys}$ and its uncertainty by means of a maximum-likelihood procedure (Walker et al. 2006), obtaining $V_{\rm sys} = -48.5 \pm 0.3$ km s^{-1}. Our estimate is in agreement with the value derived in Valenti et al. (2011; -47 ± 4 km s^{-1}) and, marginally, with that obtained by Baumgardt & Hilker (2018; -49.9 ± 0.4 km s^{-1}), while it strongly disagrees with that listed in Harris (1996; -28.1 ± 5.6 km s^{-1}).

5.3. Systemic Rotation

In previous kinematics analyses no clear signals of rotation have been detected in the external regions of NGC 6569 (e.g., Sollima et al. 2019; Vasiliev & Baumgardt 2021). However, the large sample of RV data presented here offers the opportunity to push the search for rotation further, also including the central region of the cluster. To this purpose, we used the method already adopted in several papers by our group (Lanzoni et al. 2018a; Ferraro et al. 2018b; Lanzoni et al. 2018b; Leanza et al. 2022a, 2022b).

The method is fully described in Bellazzini et al. (2012; see also Lanzoni et al. 2013) and consists in splitting the observed RV sample into two subsamples on either side of a line passing through the cluster center. The position angle (PA) of the line is then changed from 0° (north) to 180° (south), by steps of 10°

---

[9] The RV sample with the corresponding errors is available for free download at: http://www.cosmic-lab.eu/Cosmic-Lab/MIKiS_Survey.html; see Table 4 for a preview.
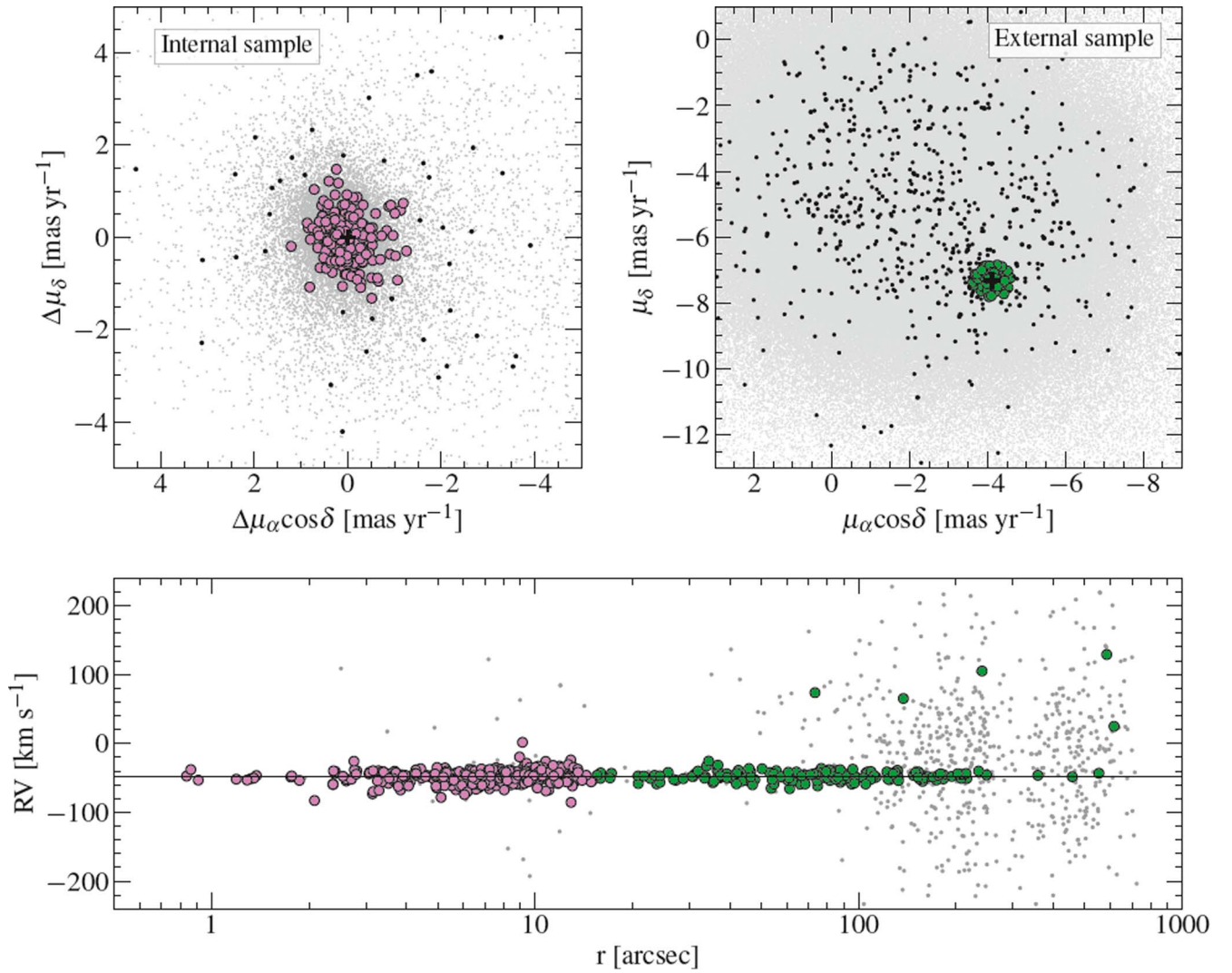
Figure 5. Top left panel: VPD of the relative PMs obtained in Saracino et al. (2019; gray dots). The member stars selected from the internal sample for the kinematic analysis of the cluster are marked with large magenta circles, while the black dots are the targets rejected as nonmembers. The black cross is centered on (0,0), thus marking the bulk motion of the cluster. Top right panel: VPD of the Gaia EDR3 data set (gray dots; only stars with $g < 18$ are plotted for visualization purposes). The green circles show the targets of the external sample selected as member stars, while those considered as field stars are indicated with black dots. The black cross marks the absolute PM of NGC 6569 (Vasiliev & Baumgardt 2021). Bottom panel: RVs of the 1292 targets of the final catalog as a function of the distance from the cluster center. The large circles mark the targets selected as cluster members on the basis of the measured PMs, color coded as in the top panels, while the gray dots are the targets rejected as field stars.
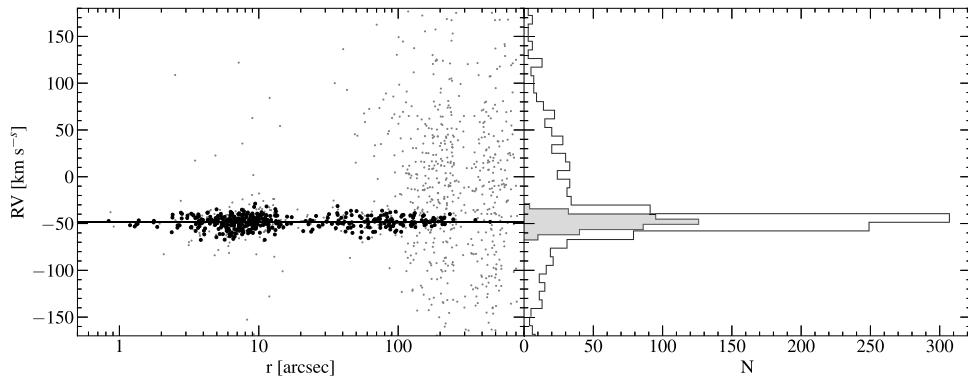
Figure 6. Left panel: RVs of the final catalog as a function of the distance from the cluster center. The black circles show the subsample of stars used for the determination of V_{sys} (solid line), while the gray dots mark the excluded targets. Right panel: the open histogram is the number distribution of the entire RV sample, while the gray histogram refers to the sample used to determine V_{sys} (black dots in the left panel).
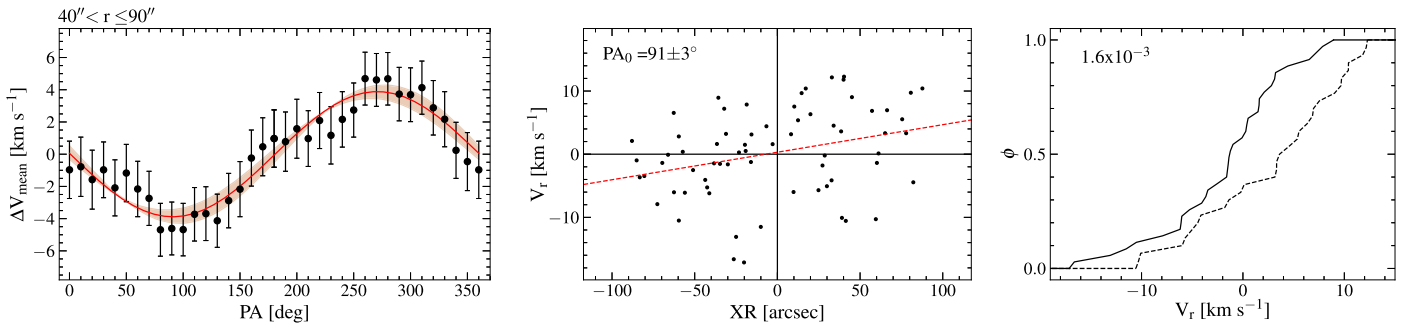
Figure 7. Diagnostic diagrams of the most significant rotation signal detected in NGC 6569 in the annular region $40'' < r < 90''$ from the cluster center. The left panel shows the difference between the mean RV on each side of a line passing through the center with a given PA as a function of PA itself. The continuous line is the sine function that best fits the observed patterns. The central panel shows the distribution of the velocities referred to V_{sys} (V_r) as a function of the projected distances from the rotation axis (XR) in arcseconds. The value of PA_0 is labeled. The red dashed line is the least square fit to the data. The right panel shows the cumulative V_r distributions for the stars with XR <0 (solid line) and for those with XR >0 (dotted line). The KS probability that the two subsamples are extracted from the same parent distribution is labeled.

and with PA $= 90°$ corresponding to the east. If the cluster is not rotating, the mean velocity of the two subsamples is the same, while in the presence of systemic rotation along the LOS, it is maximum for the value of PA corresponding to the rotation axis (PA_0). Hence, a coherent sinusoidal variation of the difference between the mean velocity of the two subsamples (ΔV_{mean}) as a function of PA can be used as diagnostic of rotation, with the maximum/minimum value of this curve providing twice the rotation amplitude (A_{rot}) and the PA of the rotation axis (PA_0). In addition, the distribution in a diagram showing the stellar RV as a function of the projected distances from the rotation axis (XR) is expected to appear highly asymmetric, with two diagonally opposite quadrants being more populated than the other two. Finally, the cumulative RV distributions of the two subsamples of stars on each side of the rotation axis are expected to be different, and the statistical significance of such difference can be evaluated through various estimators. Here we adopt the following three: the probability that the RV distributions of the two subsamples are extracted from the same parent family is estimated by means the p value of the Kolmogorov–Smirnov (KS) test, while the statistical significance of the difference between the two sample means is evaluated with both the Student's t-test and a maximum-likelihood approach.

Of course a meaningful application of this method requires a uniform distribution of the RV measures in the plane of the sky. Thus, we are forced to avoid some heavily undersampled regions and limit the analysis to the innermost $5''$, where the combination of the MUSE and SINFONI targets offers a reasonably symmetric coverage (see Figure 3), and the annular region between $15''$ and $150''$, which is sampled by FLAMES and KMOS data.

The maximum signal of rotation in these regions has been detected at $40'' < r < 90''$. This is shown in the diagnostic diagrams plotted in Figure 7, which indicate a maximum amplitude of $\sim(1.9 \pm 0.3)$ km s^{-1}, a PA of the rotation axis $PA_0 = (91 \pm 3)°$, and a p value of the KS test $p = 0.0016$, indicating that the difference between cumulative RV distributions of the two subsamples on either side of the rotation axis is significant at $\sim 2.4\sigma$. However, the number of stars observed in this region is admittedly small (67), and additional spectroscopic observations are needed to solidly confirm the presence of systemic rotation in this GC.

5.4. Velocity Dispersion Profile

As discussed in previous papers (e.g., Lanzoni et al. 2018a, 2018b; Leanza et al. 2022a), the measure of the observed RV dispersion at different radial distances from the center corresponds to the second velocity moment profile $\sigma_{II}(r)$, which is linked to the velocity dispersion profile $\sigma_P(r)$ through the following relation: $\sigma_P^2(r) = \sigma_{II}^2(r) - A_{rot}^2(r)$. Since the evidence of rotation in NGC 6569 is highly uncertain (see Section 5.3), we assume that the rotation contribution is negligible and $\sigma_P^2(r) = \sigma_{II}^2(r)$.

Hence, to determine the velocity dispersion profile of the cluster, we used the sample of RVs selected with the criteria described in Section 5.2 (only member stars, with S/N >15 and RV error <5 km s^{-1}). This has been divided into concentric radial bins with increasing distance from the center, ensuring both a proper radial sampling and a statistically sufficient number of targets (at least 25) in each bin. After a 3σ clipping procedure used to exclude the obvious outliers, we then determined the velocity dispersion value in each bin by following the maximum-likelihood method described in Walker et al. (2006; see also Martin et al. 2007; Sollima et al. 2009). The velocity dispersion uncertainties are estimated adopting the procedure described in Pryor & Meylan (1993). The results are shown in Figure 8 (blue circles) and also listed in Table 2. As it is apparent, the velocity dispersion decreases from a central value of approximately 6.5 km s^{-1} down to 3.7 km s^{-1} in the bin centered at $\sim 200''$. For the sake of comparison, in the figure we also report the profile published[10] in Baumgardt & Hilker (2018; white squares). Their two innermost points are consistent with our measures, but they are limited at $r > 30''$ and therefore do not properly characterize the central portion of the velocity dispersion profile. The outermost measure from these authors largely exceeds the dispersion velocity obtained here, probably because of residual field contamination.

6. Star Density Profile

The HST data set described in Saracino et al. (2019) offers the ideal angular resolution for determining the innermost portion ($r < 120''$) of the projected density profile of NGC 6569

---

[10] Note that the comparison has been done with published values; however, the online repository is repeatedly revised, and some updated values are in better agreement with our determinations.
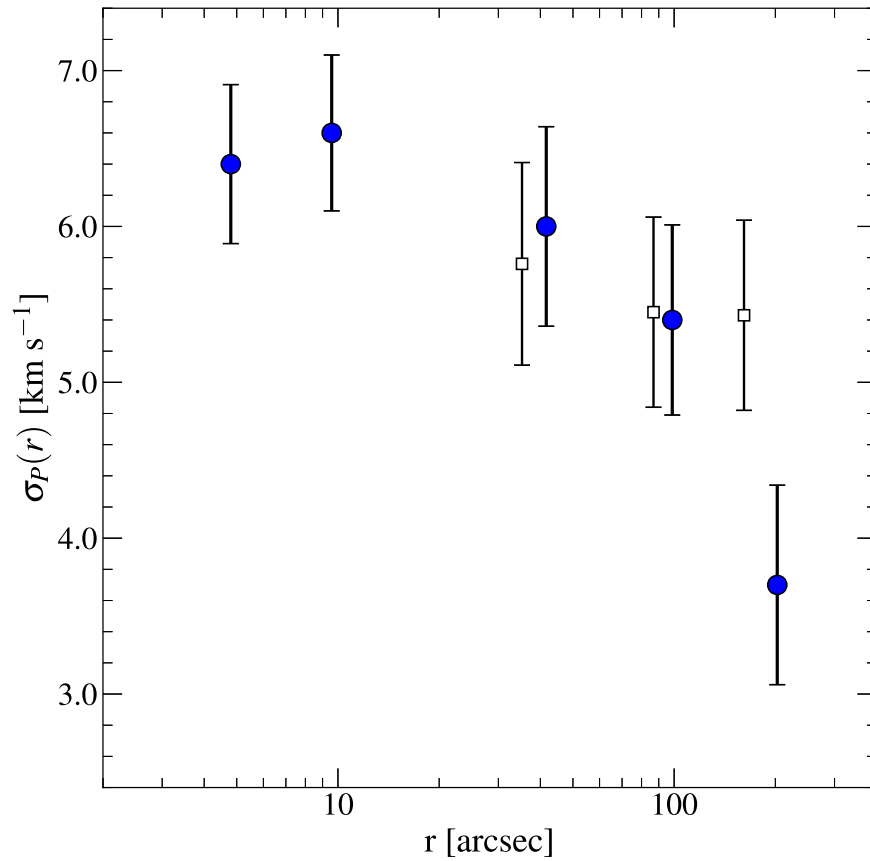
Figure 8. Velocity dispersion (second velocity moment) profile of NGC 6569 (blue circles) obtained from the measured individual RVs. For the sake of comparison, the white squares correspond to the profile published in Baumgardt & Hilker (2018).

Table 2
Velocity Dispersion Profile of NGC 6569

r_i (arcsec)	r_e (arcsec)	r_m (arcsec)	N	σ_P km s^{-1}	ϵ_{σ_P} km s^{-1}
0.01	7.00	4.80	122	6.40	0.51
7.00	15.00	9.58	131	6.60	0.50
15.00	70.00	41.56	65	6.00	0.64
70.00	150.00	98.72	50	5.40	0.61
150.00	550.00	202.63	26	3.70	0.64

Note. The table lists the internal and external radius of each radial bin (r_i and r_e, respectively), the average distance from the center of the stars within the bin (r_m), the number of stars in the bin (N), and the measured velocity dispersion and its uncertainty in the bin (σ_P and ϵ_{σ_P}, respectively).

from resolved star counts. To cover the entire extension of the system, we complemented this data set with the Gaia EDR3 catalog out to 1200″ from the cluster center. To ensure comparable levels of photometric completeness in the two data sets and sufficiently large statistics in each bin, we adopted two different magnitude cuts for the sample selection: $m_{\rm F814W} < 20.5$ for the HST/GeMS data set and $G < 18$ for the Gaia one.

According to the standard procedure used in several previous works (see, e.g., Lanzoni et al. 2010; Miocchi et al. 2013; Lanzoni et al. 2019; Pallanca et al. 2021b), we divided the sample into 20 concentric annuli centered on the $C_{\rm grav}$ and split each annulus into an appropriate number of sectors (usually four). We estimated the star surface density in each sector as

the ratio between the number of stars within the sector and the area of the sector itself. The stellar density in each annulus is then obtained as the average of the sectors densities, while their standard deviation is adopted as corresponding uncertainty. Owing to the different magnitude cuts adopted for the sample selections, the external portion of the profile (from Gaia data) has been finally shifted until it matched the last point of the HST/GeMS profile. The projected density profile thus obtained is shown in Figure 9 (open circles), where the radius associated to each annulus is the midpoint of the radial bin. The plateau at $r > 200″$ is due to the (dominant) contribution of the Galactic field, which has an essentially constant density at the small scales surveyed here. Its value has been estimated as the averaging density of the six outermost points (dashed line in Figure 9), and it has been subtracted from the observed profile. The results are shown as blue circles in Figure 9. As it is apparent, after the background subtraction, the outermost portion of the profile significantly decreases with respect to the observed one, which demonstrates that an accurate determination of the field level is essential to properly constrain the true density distribution of the system. This has the typical shape observed for most GCs, i.e., an inner flat core followed by a steadily decreasing trend (Figure 9).

7. Discussion and Conclusions

The star density and velocity dispersion profiles presented in Sections 6 and 5.4, respectively, have been obtained by using samples of stars with approximately the same mass. In addition, although no definitive conclusions on the possible existence of
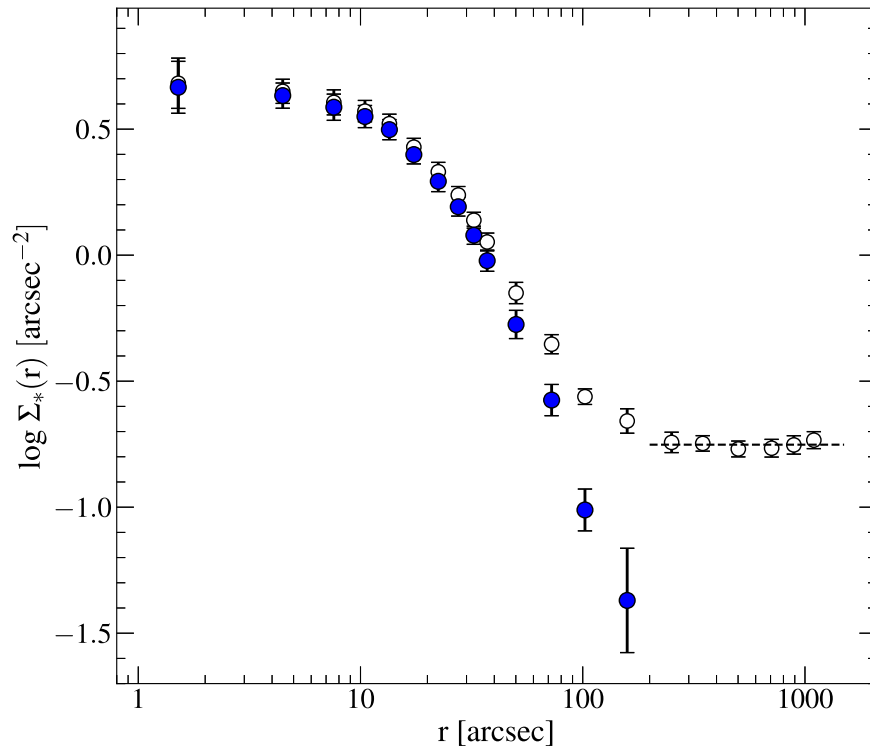
Figure 9. Observed density profile of NGC 6569 obtained from resolved star counts (open circles). The six outermost points (with $r > 200''$) define a sort of plateau and have been used to measure the density level of the background (dashed line). The blue circles show the cluster density profile obtained after subtraction of the field contribution.
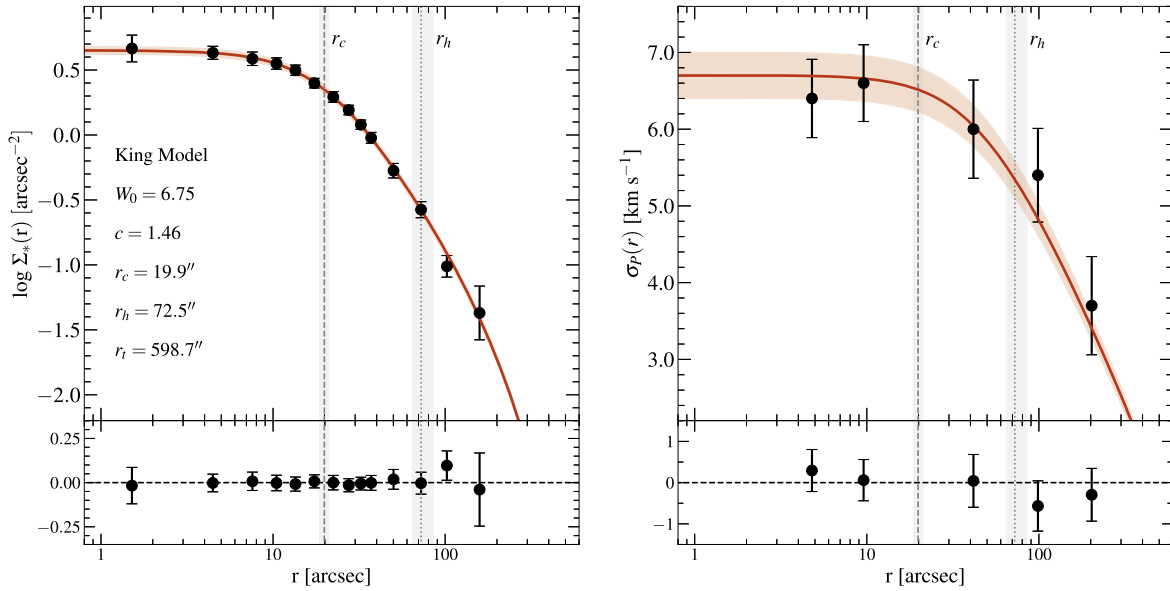

Figure 10. Best-fit King model (as derived in Section 7; red solid lines) overplotted to the star density profile (left panel) and the velocity dispersion profile (right panel) of NGC 6569. The best-fit values of the central dimensionless potential (W_0), concentration parameter (c), and core, half mass and tidal radii (r_c, r_h and r_t, respectively) are labeled in the left panel, where the dashed and dotted lines mark r_c and r_h, respectively. The shaded regions show the associated uncertainties. The bottom panels show the residuals between the model and the observations. The red shaded region in the right panel marks the 1σ confidence level on the estimate of the central velocity dispersion (see Section 7).

systemic rotation can be drawn at the moment, the results discussed in Section 5.3 suggest that the rotational velocity (if any) is negligible in this system. Hence, we determined the structural and kinematic parameters of NGC 6569 by simultaneously fitting the density and velocity dispersion profiles with single-mass, spherical, isotropic, and nonrotating King models (King 1966). These are a monoparametric family

of dynamical models, univocally characterized by the value of the dimensionless parameter W_0, which is proportional to the gravitational potential at the center of the system, or, equivalently, by the concentration parameter c, defined as $c \equiv \log(r_t/r_0)$, where r_t and r_0 are the tidal and the King radii of the model, respectively. To determine the best-fit King model to both the profiles we adopted a Markov Chain Monte

Table 3
Summary of the Main Parameters Used and Obtained in This Work for the GGC NGC 6569

Parameter	Estimated Value	Reference
Cluster center	$\alpha_{\text{J2000}} = 18^h13^m38\overset{s}{.}70$	this work
	$\delta_{\text{J2000}} = -31°49'37\overset{''}{.}13$	
Metallicity	[Fe/H] = -0.79	Valenti et al. (2011)
	[α/Fe] = $+0.4$	Valenti et al. (2011)
Cluster distance	$d = 10.1 \pm 0.2$ kpc	Saracino et al. (2019)
Dimensionless central potential	$W_0 = 6.75 \pm 0.40$	this work
Concentration parameter	$c = 1.46^{+0.12}_{-0.11}$	this work
Core radius	$r_c = 19\overset{''}{.}9 \pm 1.2 = 0.97$ pc	this work
Three-dimensional half-mass–radius	$r_\text{h} = 72\overset{''}{.}5^{+12.9}_{-7.9} = 3.55$ pc	this work
Effective radius	$r_\text{eff} = 54\overset{''}{.}1^{+9.3}_{-5.7} = 2.65$ pc	this work
Tidal radius	$r_t = 589\overset{''}{.}7^{+167.9}_{-109.3} = 28.88$ pc	this work
Systemic velocity	$V_\text{sys} = -48.5 \pm 0.3$ km s^{-1}	this work
Central velocity dispersion	$\sigma_0 = 6.7 \pm 0.3$ km s^{-1}	this work
Absolute proper motions	$\mu_\alpha \cos\delta = -4.125$ mas yr^{-1}	Vasiliev & Baumgardt (2021)
	$\mu_\delta = -7.315$ mas yr^{-1}	
Total mass	$M = 1.72^{+0.20}_{-0.18} \times 10^5 M_\odot$	this work
Central relaxation time	$\log(t_\text{rc}) = 8.3$ [in yr]	this work
Half-mass relaxation time	$\log(t_\text{rh}) = 9.2$ [in yr]	this work

Carlo approach by means of the emcee algorithm (Foreman-Mackey et al. 2013). We assumed uniform priors on the parameters of the fit, obtaining the posterior probability distribution functions (PDFs) for the characteristic parameters of the King models and for the central velocity dispersion, σ_0. For each parameter, the PDF median has been adopted as best-fit value, while the 16th and 84th percentiles of the posterior PDF have been used to estimate the 1σ uncertainty.

The resulting best-fit King model is shown overplotted to the observed density and velocity dispersion profiles in Figure 10 (red lines), where the residuals between the model and the observations are also shown in the bottom panels. A very good agreement is apparent, thus indicating that both the structure (as it is often the case for GGCs) and the internal kinematics of NGC 6569 are well consistent with the King model expectations. The best-fit model is characterized by $W_0 = 6.75$ (which corresponds to $c = 1.46$) and a core radius $r_c = 19\overset{''}{.}9$, corresponding to $\sim$1 pc at the distance of the cluster ($d = 10.1$ kpc; Saracino et al. 2019). The half mass and tidal radii are, respectively, $r_\text{h} = 72\overset{''}{.}5$ and $r_t = 589\overset{''}{.}7$, while the effective radius (i.e., the radial distance at which the projected density, or the surface brightness, halves the central value) is $r_\text{eff} = 54\overset{''}{.}1$. For the central velocity dispersion we obtained $\sigma_0 = 6.7 \pm 0.3$ km s^{-1}. The best-fit values and the uncertainties of each parameter are listed in Table 3.

Comparing our estimates with the results obtained from the surface brightness profile by McLaughlin & van der Marel (2005; which are also the values quoted in Harris 1996), we find consistent values within the uncertainties: in fact, after conversion from parsecs to arcseconds using the cluster distance provided in that paper ($d = 10.7$ kpc), these authors quote: $W_0 = 6.20 \pm 0.2$,

$c = 1.31 \pm 0.05$, $r_c = 21''$, $r_\text{eff} = 48''$, and $r_t = 461''$. Within the errors, our values are in agreement also with those of Baumgardt & Hilker (2018; $r_c = 20\overset{''}{.}74$ and $r_h = 78\overset{''}{.}86$, converted into arcseconds using the cluster distance quoted in their paper: $d = 12.0$ kpc). We remark, however, that this comparison is neither obvious nor rigorous because Baumgardt & Hilker (2018) derive these quantities from N-body simulations instead of fitting the observations with King models. As for the estimate of σ_0, our value is lower than that quoted in Baumgardt & Hilker (2018; $\sigma_0 \sim 7.5$ km s^{-1}). This discrepancy is likely due to the fact that the velocity dispersion profile used in that work is poorly constrained (see Figure 8 and also Figure E12 in Baumgardt & Hilker 2018).

Under the (well-motivated) assumption of a King model structure and by adopting the obtained value of σ_0, we estimated the total mass of the cluster as $M = 166.5 r_0 \mu / \beta$ (Majewski et al. 2003), where r_0 is the King radius, μ is a scaling parameter depending on the King concentration c as $\log \mu = -0.14192 c^4 + 1.15592 c^3 - 3.16183 c^2 + 4.21004 c - 1.00951$ (Djorgovski 1993), and $\beta = 1/\sigma_0^2$ (Richstone & Tremaine 1986). The uncertainty has been estimated as the dispersion of the mass values resulting from 1000 Monte Carlo simulations, run by adopting appropriate normal distributions for c, r_0, and σ_0 (see Leanza et al. 2022a). The resulting total mass is $M = 1.72^{+0.20}_{-0.18} \times 10^5 M_\odot$. This is lower than the value obtained by Baumgardt & Hilker (2018; $3.02 \pm 0.36 \times 10^5 M_\odot$) from N-body simulations, presumably due to the different velocity dispersion profile used as a constraint, other than the different assumptions and methods adopted in the two works (for instance, Baumgardt & Hilker 2018 adopt a 20% larger distance of the cluster than assumed here, and they compare the observations with a library of N-body simulations). Finally, by adopting the structural parameters determined here, the total mass and the cluster distance of Saracino et al. (2019), we estimated the central and half-mass relaxation times (t_rc and t_rh) from Equations (10) and (11) of Djorgovski (1993), respectively. To estimate the central relaxation time (in years), we used:

$$t_\text{rc} = \frac{0.834 \times 10^7}{\ln(0.4N)} \frac{\rho_{0,M}^{1/2} r_c^3}{m}, \qquad (2)$$

where N is the total number of stars, $\rho_{0,M}$ is the central mass density, and m is the average stellar mass. For the half-mass relaxation time (in years), we adopted:

$$t_\text{rh} = \frac{2.055 \times 10^6}{\ln(0.4N)} \frac{M^{1/2} r_h^3}{m}. \qquad (3)$$

We found $\log(t_\text{rc}) = 8.3$ and $\log(t_\text{rh}) = 9.2$, which are roughly consistent with the values quoted in the Harris (1996; 8.38 and 9.05, respectively) catalog, consistent with the fact that also the differences in terms of structural parameters and cluster distance are small. These values suggest that NGC 6569 is in an intermediate stage of its dynamical evolution although dedicated investigations of this issue (see, e.g., Ferraro et al. 2018 and Cadelano et al. 2020; Bhat et al. 2022, 2023) are needed to properly confirm it.

Acknowledgments

Appendix
Kinematic Catalog

Table 4 provides the kinematic catalog of the quality selected stars (S/N > 15 and RV error < 5 km s^{-1}) in NGC 6569.

Table 4
Kinematic Catalog

id	α (deg)	δ (deg)	m_{F555W}	m_{F814W}	J	K	RV (km s^{-1})	ϵ_{RV} (km s^{-1})
1	273.4090654	−31.8265292	15.17	12.64	11.23	10.07	−60.6	0.3
2	273.4110241	−31.8276114	15.18	12.69	11.26	10.11	−59.3	0.3
3	273.4094891	−31.8281725	15.25	12.76	11.36	10.25	−47.1	0.3
4	273.4088372	−31.8290447	15.22	13.01	11.57	10.41	−37.9	0.8
5	273.4109841	−31.8251144	15.53	13.43	12.12	11.15	−44.9	0.7
6	273.4112084	−31.8295540	16.01	14.03	12.81	11.92	−44.6	0.8
7	273.4121423	−31.8295264	15.86	13.96	12.90	12.00	−46.2	0.7
8	273.4080336	−31.8266938	16.29	14.31	13.01	12.07	−47.2	1.1
9	273.4117724	−31.8302748	16.22	14.23	13.02	12.11	84.2	0.9
10	273.4098361	−31.8293371	16.49	14.52	13.18	12.29	−55.5	1.0
...	...	...	...	...	...	...	...	...

Note. First ten rows of the kinematic catalog, reporting the identification number, the absolute coordinates, the optical and NIR magnitudes (if available), and the measured line-of-sight velocities and errors for all the stars surviving the quality selection criteria. No membership selection is applied. The entire table is provided.

(This table is available in its entirety in machine-readable form.)

ORCID iDs

Cristina Pallanca ● https://orcid.org/0000-0002-7104-2107
Silvia Leanza ● https://orcid.org/0000-0001-9545-5291
Francesco R. Ferraro ● https://orcid.org/0000-0002-2165-8528
Barbara Lanzoni ● https://orcid.org/0000-0001-5613-4938
Emanuele Dalessandro ● https://orcid.org/0000-0003-4237-4601
Mario Cadelano ● https://orcid.org/0000-0002-5038-3914
Enrico Vesperini ● https://orcid.org/0000-0003-2742-6872
Livia Origlia ● https://orcid.org/0000-0002-6040-5849
Alessio Mucciarelli ● https://orcid.org/0000-0001-9158-8580
Elena Valenti ● https://orcid.org/0000-0002-6092-7145

References

Arsenault, R., Madec, P.-Y., Hubin, N., et al. 2008, Proc. SPIE, 7015, 701524
Bacon, R., Accardo, M., Adjali, L., et al. 2010, Proc. SPIE, 7735, 773508
Barbuy, B., Chiappini, C., & Gerhard, O. 2018, ARA&A, 56, 223
Barnard, E. E., Frost, E. B., & Calvert, M. R. 1927, A Photographic Atlas of Selected Regions of the Milky Way (Washington, DC: Carnegie Inst.)
Baumgardt, H., & Hilker, M. 2018, MNRAS, 478, 1520
Bellazzini, M., Bragaglia, A., Carretta, E., et al. 2012, A&A, 538, A18
Bhat, B., Lanzoni, B., Ferraro, F. R., et al. 2022, ApJ, 926, 118
Bhat, B., Lanzoni, B., Ferraro, F. R., et al. 2023, ApJ, 945, 164
Bica, E., Bonatto, C., Barbuy, B., et al. 2006, A&A, 450, 105
Cadelano, M., Dalessandro, E., Ferraro, F. R., et al. 2017a, ApJ, 836, 170
Cadelano, M., Dalessandro, E., Webb, J. J., et al. 2020, MNRAS, 499, 2390
Cadelano, M., Ferraro, F. R., Dalessandro, E., et al. 2022, ApJ, 941, 69
Cadelano, M., Pallanca, C., Ferraro, F. R., et al. 2017b, ApJ, 844, 53
Cadelano, M., Saracino, S., Dalessandro, E., et al. 2020, ApJ, 895, 54
Dalessandro, E., Crociati, C., Cignoni, M., et al. 2022, ApJ, 940, 170
Deras, D., Cadelano, M., Ferraro, F. R., et al. 2023, ApJ, 942, 104
Djorgovski, S. 1993, in ASP Conf. Ser. 50, Structure and Dynamics of Globular Clusters, ed. S. G. Djorgovski & G. Meylan (San Francisco, CA: ASP), 373
Eisenhauer, F., Abuter, R., Bickert, K., et al. 2003, Proc. SPIE, 4841, 1548
Ferraro, F. R., Dalessandro, E., Mucciarelli, A., et al. 2009, Natur, 462, 483
Ferraro, F. R., Lanzoni, B., Raso, S., et al. 2018, ApJ, 860, 36
Ferraro, F. R., Massari, D., Dalessandro, E., et al. 2016, ApJ, 828, 75
Ferraro, F. R., Mucciarelli, A., Lanzoni, B., et al. 2018a, ApJ, 860, 50
Ferraro, F. R., Mucciarelli, A., Lanzoni, B., et al. 2018b, Msngr, 172, 18
Ferraro, F. R., Pallanca, C., Lanzoni, B., et al. 2015, ApJL, 807, L1
Ferraro, F. R., Pallanca, C., Lanzoni, B., et al. 2021, NatAs, 5, 311
Fétick, R. J. L., Fusco, T., Neichel, B., et al. 2019, A&A, 628, A99
Foreman-Mackey, D., Hogg, D. W., Lang, D., et al. 2013, PASP, 125, 306
Freudling, W., Romaniello, M., Bramich, D. M., et al. 2013, A&A, 559, A96
Gaia Collaboration, Brown, A. G. A., Vallenari, A., et al. 2021, A&A, 649, A1
Gaia Collaboration, Prusti, T., de Bruijne, J. H. J., et al. 2016, A&A, 595, A1
Göttgens, F., Kamann, S., Baumgardt, H., et al. 2021, MNRAS, 507, 4788
Harris, W. E. 1996, AJ, 112, 1487
Johnson, C. I., Rich, R. M., Caldwell, N., et al. 2018, AJ, 155, 71
Johnson, C. I., Rich, R. M., Simion, I. T., et al. 2022, MNRAS, 515, 1469
Kamann, S., Husser, T.-O., Brinchmann, J., et al. 2016, A&A, 588, A149
Kamann, S., Wisotzki, L., & Roth, M. M. 2013, A&A, 549, A71
King, I. R. 1966, AJ, 71, 64
Kurucz, R. L. 2005, MSAIS, 8, 14
Lanzoni, B., Ferraro, F. R., Dalessandro, E., et al. 2010, ApJ, 717, 653
Lanzoni, B., Ferraro, F. R., Dalessandro, E., et al. 2019, ApJ, 887, 176
Lanzoni, B., Ferraro, F. R., Mucciarelli, A., et al. 2018a, ApJ, 861, 16
Lanzoni, B., Ferraro, F. R., Mucciarelli, A., et al. 2018b, ApJ, 865, 11
Lanzoni, B., Mucciarelli, A., Origlia, L., et al. 2013, ApJ, 769, 107
Lapenna, E., Origlia, L., Mucciarelli, A., et al. 2015, ApJ, 798, 23
Leanza, S., Pallanca, C., Ferraro, F. R., et al. 2022a, ApJ, 929, 186
Leanza, S., Pallanca, C., Ferraro, F. R., et al. 2022b, ApJ, 929, 186
Libralato, M., Bellini, A., van der Marel, R. P., et al. 2018, ApJ, 861, 99
Libralato, M., Bellini, A., Vesperini, E., et al. 2022, ApJ, 934, 150
Majewski, S. R., Skrutskie, M. F., Weinberg, M. D., et al. 2003, ApJ, 599, 1082
Marchetti, T., Johnson, C. I., Joyce, M., et al. 2022, A&A, 664, A124
Martin, N. F., Ibata, R. A., Chapman, S. C., et al. 2007, MNRAS, 380, 281
Massari, D., Bellini, A., Ferraro, F. R., et al. 2013, ApJ, 779, 81
Massari, D., Mucciarelli, A., Ferraro, F. R., et al. 2014, ApJ, 795, 22
McLaughlin, D. E., & van der Marel, R. P. 2005, ApJS, 161, 304
Miocchi, P., Lanzoni, B., Ferraro, F. R., et al. 2013, ApJ, 774, 151
Montegriffo, P., Ferraro, F. R., Fusi Pecci, F., et al. 1995, MNRAS, 276, 739
Ness, M., Freeman, K., Athanassoula, E., et al. 2013, MNRAS, 430, 836
Origlia, L. 2014, in Formation and Evolution of the Galactic Bulge, Proc. Conf., 7
Origlia, L., Ferraro, F. R., Fusi Pecci, F., et al. 1997, A&A, 321, 859
Origlia, L., Massari, D., Rich, R. M., et al. 2013, ApJL, 779, L5
Origlia, L., Mucciarelli, A., Fiorentino, G., et al. 2019, ApJ, 871, 114
Origlia, L., & Rich, R. M. 2004, AJ, 127, 3422
Origlia, L., Rich, R. M., & Castro, S. 2002, AJ, 123, 1559
Origlia, L., Rich, R. M., & Castro, S. M. 2001, AAS Meeting 199, 56.16
Origlia, L., Rich, R. M., Ferraro, F. R., et al. 2011, ApJL, 726, L20
Origlia, L., Valenti, E., & Rich, R. M. 2005, MNRAS, 356, 1276
Ortolani, S., Bica, E., & Barbuy, B. 2001, A&A, 374, 564
Pallanca, C., Ferraro, F. R., Lanzoni, B., et al. 2019, ApJ, 882, 159
Pallanca, C., Ferraro, F. R., Lanzoni, B., et al. 2021a, ApJ, 917, 92
Pallanca, C., Lanzoni, B., Ferraro, F. R., et al. 2021b, ApJ, 913, 137
Pasquini, L., Avila, G., Blecha, A., et al. 2002, Msngr, 110, 1
Pryor, C., & Meylan, G. 1993, in ASP Conf. Ser. 50, Structure and Dynamics of Globular Clusters, ed. S. G. Djorgovski & G. Meylan (San Francisco, CA: ASP), 357
Raso, S., Libralato, M., Bellini, A., et al. 2020, ApJ, 895, 15
Rich, R. M. 2013, in Planets, Stars and Stellar Systems, ed. T. D. Oswalt & G. Gilmore, Vol. 5 (Dordrecht: Springer), 271
Richstone, D. O., & Tremaine, S. 1986, AJ, 92, 72
Saracino, S., Dalessandro, E., Ferraro, F. R., et al. 2015, ApJ, 806, 152
Saracino, S., Dalessandro, E., Ferraro, F. R., et al. 2016, ApJ, 832, 48
Saracino, S., Dalessandro, E., Ferraro, F. R., et al. 2019, ApJ, 874, 86
Sbordone, L., Bonifacio, P., Castelli, F., et al. 2004, MSAIS, 5, 93
Sharples, R., Bender, R., Agudo Berbel, A., et al. 2013, Msngr, 151, 21
Skrutskie, M. F., Cutri, R. M., Stiening, R., et al. 2006, AJ, 131, 1163
Sollima, A., Baumgardt, H., & Hilker, M. 2019, MNRAS, 485, 1460
Sollima, A., Bellazzini, M., Smart, R. L., et al. 2009, MNRAS, 396, 2183
Ströbele, S., La Penna, P., Arsenault, R., et al. 2012, Proc. SPIE, 8447, 844737
Tonry, J., & Davis, M. 1979, AJ, 84, 1511
Valenti, E., Ferraro, F. R., & Origlia, L. 2007, AJ, 133, 1287
Valenti, E., Ferraro, F. R., & Origlia, L. 2010, MNRAS, 402, 1729
Valenti, E., Origlia, L., & Ferraro, F. R. 2005, MNRAS, 361, 272
Valenti, E., Origlia, L., & Rich, R. M. 2011, MNRAS, 414, 2690
Vasiliev, E., & Baumgardt, H. 2021, MNRAS, 505, 5978
Walker, M. G., Mateo, M., Olszewski, E. W., et al. 2006, AJ, 131, 2114
Weilbacher, P. M., Palsa, R., Streicher, O., et al. 2020, A&A, 641, A28
Zoccali, M., & Valenti, E. 2016, PASA, 33, e025